

Amorphous MoS₂ Photodetector with Ultra-Broadband Response

Zhongzheng Huang,^{†,‡} Tianfu Zhang,^{†,‡} Junku Liu,[§] Lihui Zhang,^{†,‡} Yuanhao Jin,^{†,‡} Jiaping Wang,^{†,‡} Kaili Jiang,^{†,‡} Shoushan Fan,^{†,‡} and Qunqing Li^{*,†,‡}

[†]Department of Physics, State Key Laboratory of Low-Dimensional Quantum Physics and Tsinghua-Foxconn Nanotechnology Research Center, Tsinghua University, Beijing 100084, P. R. China

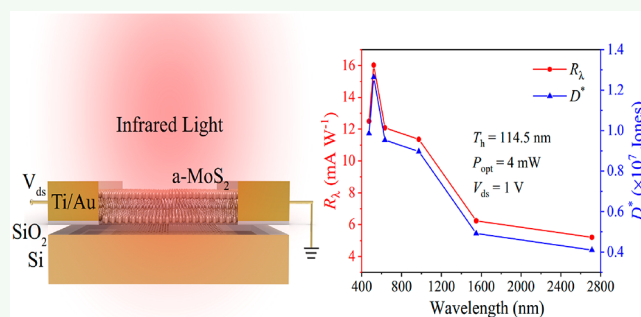
[‡]Collaborative Innovation Center of Quantum Matter, Beijing 100084, P. R. China

[§]Nanophotonics and Optoelectronics Research Center, Qian Xuesen Laboratory of Space Technology, China Academy of Space Technology, Beijing 100094, P. R. China

Supporting Information

ABSTRACT: Photodetectors with the ability to detect light over a broad spectral range at room temperature (RT) are attracting considerable attention because of their wide range of potential applications in electronic and optoelectronic devices. In this work, an ultrabroadband photodetector design based on amorphous MoS₂ (a-MoS₂) prepared by magnetron sputtering is reported for the first time. In association with a narrow bandgap of 0.196 eV that originated from defects, these devices have realized an ultrabroadband photodetection range from 473 to 2712 nm with photoresponsivity as high as 47.5 mA W⁻¹, which is comparable with most existing broadband photodetectors. Unlike many other photodetectors, which require complex manufacturing processes and rare photoactive materials that are difficult to obtain or fabricate, the amorphous MoS₂ photodetector based on the magnetron sputtering technique offers easy and rapid fabrication, ultralow cost, a large-scale manufacturing capability, no detrimental effects on the environment or humans, and compatibility with semiconductor processing. These advantages indicate that the proposed photodetector has significant potential for electronic and optoelectronic applications and offers a new path for development of ultrabroadband photodetectors.

KEYWORDS: amorphous MoS₂, ultrabroadband, defect, photodetection, magnetron sputtering technique



1. INTRODUCTION

Photodetectors, with their ability to convert light into electrical signals, have a wide range of potential applications, including imaging, sensing, and communications.^{1–9} The semiconductor material is one of the most important components of photodetectors and the detectable spectrum range depends on the semiconductor's energy band gap.^{10–18} To date, photons from the ultraviolet, visible, near-infrared, and mid-infrared regimes have been detected using semiconductors with different band gaps, such as GaN, Si, InGaAs and HgCdTe, respectively.^{19–22} For detection in the far-infrared regime, thermosensitive materials such as VO_x are commonly used.²³ However, with soaring demand in applications including imaging, communications and broadband detection, photodetectors with broadband responses at room temperature are urgently required.^{24–27} HgCdTe is the main narrow bandgap semiconductor used to detect spectral ranges of over 2500 nm, but its low temperature operation, unstable structure, and toxic element content limit its applications.

Graphene is a gapless 2D material and emerged as a promising candidate to achieve a broadband spectral response, but its low absorption (2.3%) and photoresponsivity (≈ 1 mA W⁻¹) are major problems for such applications.²⁸ Hybrid-

ization of graphene with quantum dots can improve its photoresponsivity remarkably, but because the quantum dots become the photoactive materials rather than graphene, the hybridization method limits the detectable spectral range.²⁹ Unlike graphene, molybdenum disulfide (MoS₂) shows stronger photon–electron interactions and higher absorption in the spectral range within its bandgap, thus indicating that MoS₂ is a promising light detection material.^{30,31} The first reported single-layer MoS₂ phototransistor realized photoresponsivity of 0.42 mA W⁻¹ at a wavelength of 550 nm,³² and a maximum photoresponsivity of 880 A W⁻¹ at a wavelength of 561 nm was subsequently realized by improving the mobility, contact quality and positioning technique.³³ However, the photoresponsivity decreased sharply to zero when the wavelength increased to 680 nm, which means that this type of MoS₂ phototransistor has a narrow photoresponse range. While the bandgap of crystalline MoS₂ can be tuned from 1.8 to 1.2 eV Although increasing its thickness from a single layer to bulk level, it is still far away from realizing a broadband

Received: April 22, 2019

Accepted: June 24, 2019

Published: June 24, 2019

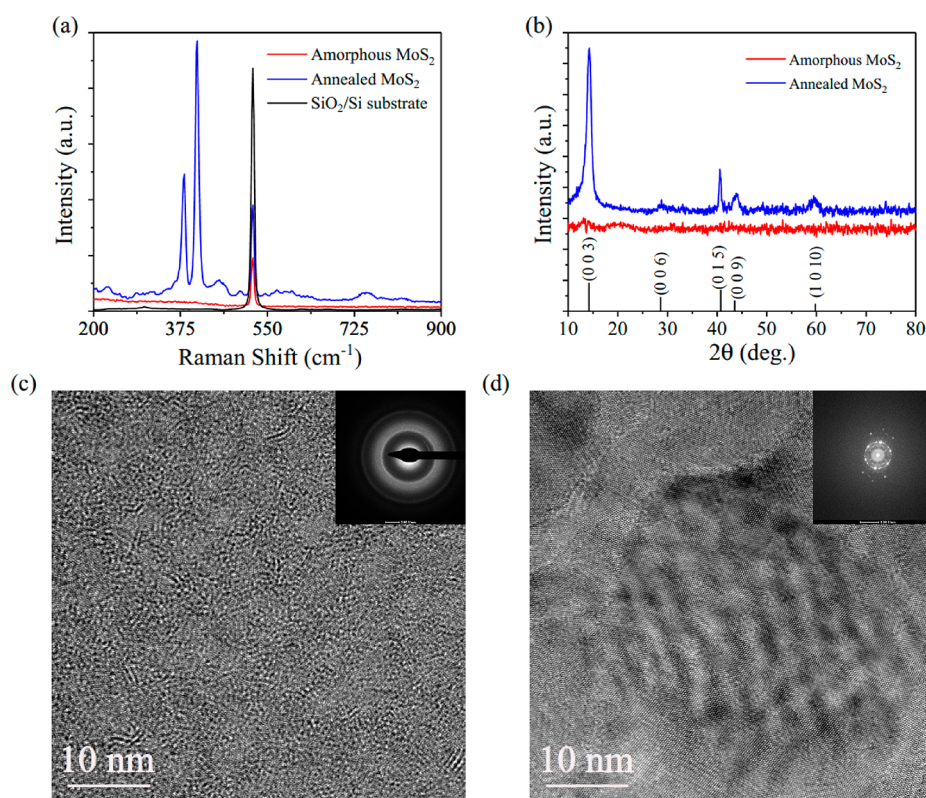


Figure 1. Raman, XRD, and TEM characterizations of amorphous MoS₂. (a) Raman spectra of the SiO₂/Si substrate and the MoS₂ sample before and after annealing. (b) XRD patterns of the MoS₂ sample before and after annealing. (c, d) TEM characterization of the MoS₂ sample before and after annealing.

response for MoS₂ photodetectors. Recently, control of the deviation from perfection of the atomic lattice has been considered as a new way to break through the intrinsic MoS₂ bandgap. A broadband polycrystalline MoS_{1.89} photodetector prepared by pulsed laser deposition (PLD) was reported that realized a spectral response from 445 to 2717 nm with maximum photoresponsivity of approximately 32 mA W⁻¹ at 1550 nm.³⁴ After that, a layered MoS_{2.15} prepared by PLD was reported to have an engineered bandgap of 0.13 eV and achieve an ultrabroadband photoresponse from 445 to 9536 nm with photoresponsivity of 21.8 mA W⁻¹;³⁵ however, the preparation process required high substrate temperatures of up to 600 °C or more and had higher costs than the magnetron sputtering technique. Another approach involves construction of MoS₂ photodetectors driven by ferroelectrics, which have a spectral response up to 1550 nm but quite low photoresponsivity.³⁶ PbS nanocrystal-based photodetectors have been reported with high photoresponsivity of approximately 0.37 A W⁻¹ at $\lambda = 2 \mu\text{m}$, but it is difficult to broaden their photoresponse range over 2.5 μm , which will require rigorous preparation technology to fabricate PbS nanocrystals with larger diameters.³⁷

In this work, we present an amorphous MoS₂ photodetector prepared by magnetron sputtering that exhibits an ultrabroadband response range from 473 to 2712 nm, which is much wider than the photoresponse ranges of traditional InGaAs and Ge photodetectors (800 to 1700 nm and 800 to 1800 nm, respectively).³⁷ This photodetector achieves photoresponsivity as high as 47.5 mA W⁻¹ at a wavelength of 1550 nm, which is much higher than that of traditional single-layer MoS₂ photodetectors, which have photoresponsivity of

approximately 7.5 mA W⁻¹ at a wavelength of 550 nm and require high gate voltages.³² Our photodetector exhibits much higher photoresponsivity and has a much wider detectable spectrum, ranging from 473 to 2712 nm. Unlike many other photodetectors that require complex manufacturing processes and rare photoactive materials, which makes it very difficult to realize large-scale production, these amorphous MoS₂ photodetectors fully realize the advantages of the magnetron sputtering technique to achieve fabrication on a large scale with high yield and ultralow cost.

2. RESULTS AND DISCUSSION

Because of the advantages of magnetron sputtering, amorphous MoS₂ can be deposited easily on many types of substrates, including quartz and SiO₂/Si substrate. Details of the fabrication and characterization of amorphous MoS₂ are presented in Figures 1 and Figure S1. To confirm the structures of the prepared MoS₂ samples, Raman spectroscopy, transmission electron microscopy (TEM) and X-ray diffraction (XRD) characterization were implemented. Figure 1a presents the Raman spectrum for an excitation wavelength of 514 nm. From this Raman spectrum, it is obvious that the typical E_{2g} and A_{1g} vibration modes of MoS₂ did not appear until the sample was annealed at 800 °C for 40 min. Figure 1b shows the XRD pattern of the MoS₂ sample, which also showed no typical MoS₂ peak until the sample was annealed at 800 °C for 40 min. Furthermore, to gain a better understanding of the sample structure, TEM characterization of the sample before and after annealing was implemented, with results as shown in Figure 1c, d, respectively. Figure 1c clearly shows that there is no ordered and periodic structure in the pristine sample,

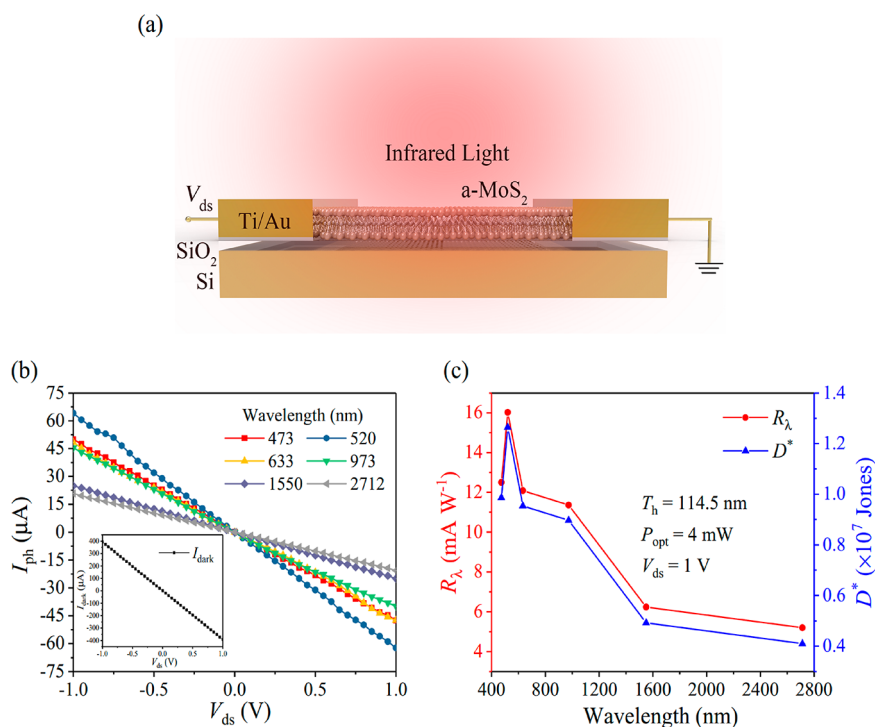


Figure 2. Layout and ultrabroadband response of a-MoS₂ photodetector. (a) Schematic view of amorphous MoS₂ photodetector with a pair of 10/40 nm Ti/Au electrodes. (b) Photocurrents generated at various wavelengths from 473 to 2717 nm, acquired over a bias voltage range from -1 to 1 V. The inset is the dark current. (c) Corresponding photoresponsivity (R_{λ}) and detectivity (D^*), acquired at $V_{ds} = 1$ V and plotted as a function of wavelength.

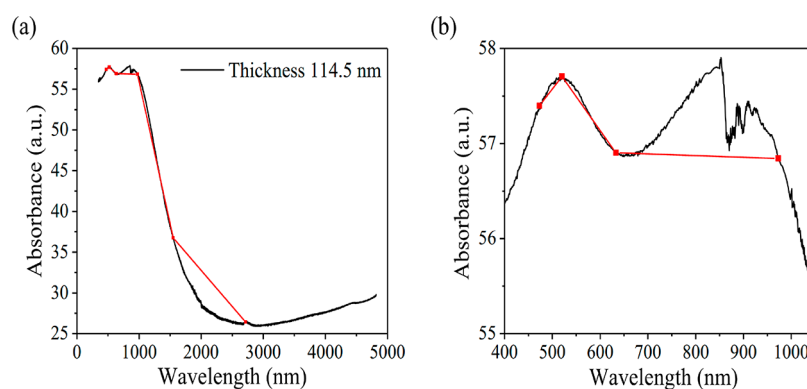


Figure 3. Absorption spectrum of a-MoS₂. (a) Absorption spectrum of an amorphous MoS₂ sample with thickness $T_h = 114.5$ nm, which shows an upward trend even in the range above $2.7 \mu\text{m}$. Six special points, with abscissa values of 473, 520, 633, 973, 1550, and 2712 nm, have been selected and marked. (b) A partial enlarged view for the wavelength range from 400 to 1050 nm.

whereas the inset shows the corresponding fast Fourier transform (FFT) result, which further proves that the sample has an amorphous structure. After annealing at 800°C for 40 min, we can clearly see the grain boundary in the sample along with ordered and periodic structures within the different grains (Figure 1d). The FFT pattern in the inset further demonstrates the presence of lattices within the annealed MoS₂ sample. The Raman spectroscopy, TEM and XRD characterizations all explicitly demonstrate that the pristine MoS₂ sample that was prepared by magnetron sputtering is amorphous.

To enable spectral response characterization of the amorphous MoS₂ photodetector, we used different light sources at wavelengths ranging from 473 to 2712 nm to illuminate the devices. Figure 2a shows a schematic view of the amorphous MoS₂ photodetector with a pair of 10/40 nm Ti/Au electrodes (Ti/Au electrodes provide the optimal contact

with amorphous MoS₂ among six types of metal electrodes that were investigated, as shown in Figure S2). We recorded the photocurrent I_{ph} (where $I_{ph} = I_{illumination} - I_{dark}$) at different wavelengths with the same incident power of $P_{opt} = 4$ mW, as shown in Figure 2b. The linear and symmetrical photocurrent versus bias voltage ($I_{ph} - V_{ds}$) curves demonstrate the ohmic-like contact characteristics. Photoresponsivity (R_{λ}) and detectivity (D^*) are two of the most important figures of merit for evaluation of the ability to convert light signals into electrical signals and detect light signals from noise at a specific wavelength. R_{λ} and D^* are expressed as

$$R_{\lambda} = \frac{I_{ph}}{P_{opt}} \quad (1)$$

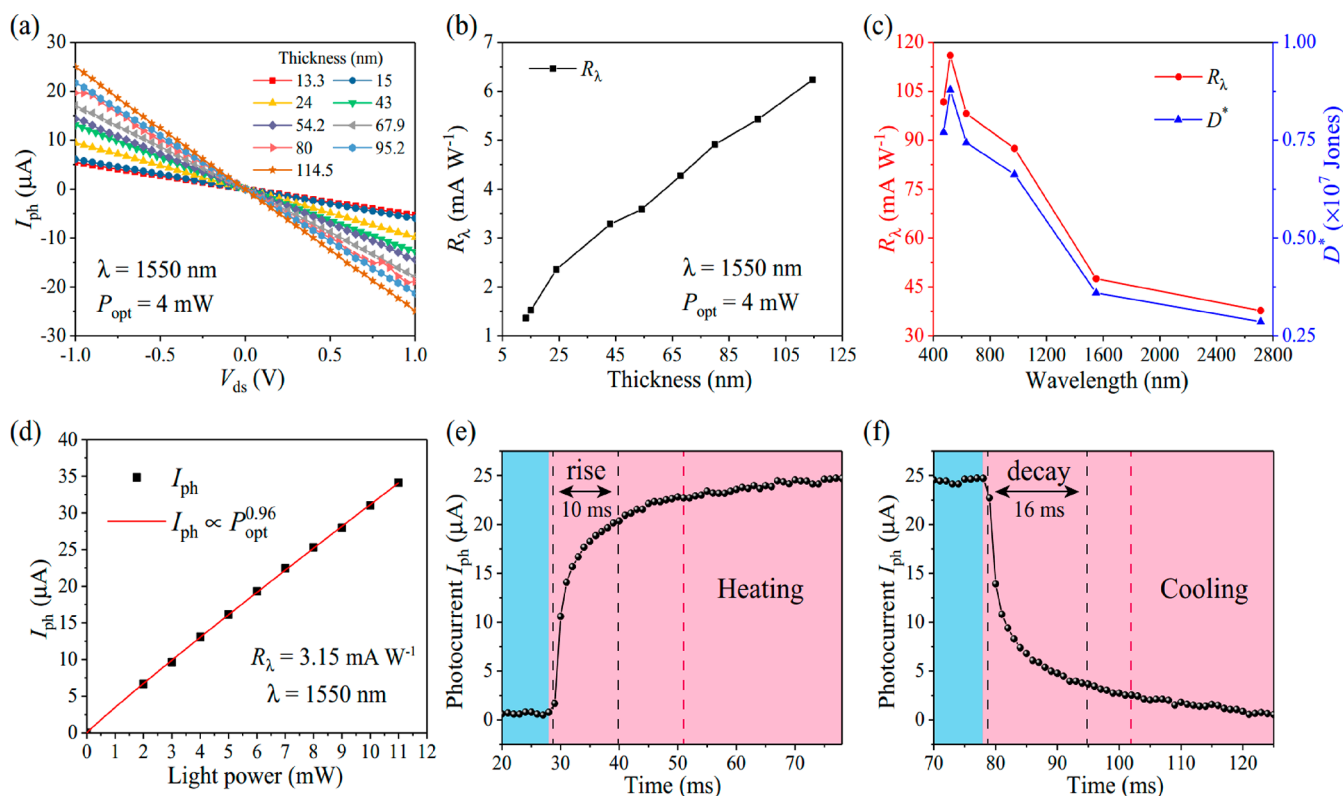


Figure 4. Characterization of a-MoS₂ photodetector. (a) Photocurrents of amorphous MoS₂ samples with various thicknesses plotted as a function of bias voltage from -1 to 1 V, acquired under illumination at a wavelength of 1550 nm with incident power of 4 mW. (b) Corresponding photoresponsivity (R_λ) results versus thickness, acquired at $V_{ds} = 1$ V. (c) Photoresponsivity (R_λ) and detectivity (D^*) plotted as a function of wavelength. The photoresponsivity reaches 47.5 mA W⁻¹ at $V_{ds} = -10$ V, $\lambda = 1550$ nm. (d) Photocurrent generated at 1550 nm, which increases in proportion to the increment in the light power, thus demonstrating excellent photocurrent capability. (e, f) Time-resolved photoresponses of the device acquired at $V_{ds} = 1$ V. The rise and decay times are 10 and 16 ms, respectively.

$$D^* = \frac{R_\lambda \sqrt{S}}{I_n} \quad (2)$$

where P_{opt} is the incident light power, S is the photosensitive area, I_n is the noise spectral density and q is the unit charge (equal to 1.6×10^{-19} C). The noise spectral density of the photodetector was measured under a bias voltage of 1 V, with result as shown in Figure S3. At 1 Hz, we get $I_n = 1.88 \times 10^{-11}$ A Hz^{-1/2}. R_λ and D^* were determined based on eq 1 and 2 and are shown in Figure 2c. R_λ and D^* obviously show the same trends as the wavelength increases and both reach maximum values at a wavelength of 520 nm, with values of 16 mA W⁻¹ and 1.26×10^7 Jones, respectively, acquired at a bias voltage of $V_{ds} = 1$ V. Although it has been reported that the maximum detectable wavelength of PbS and PbSe bulk photodetectors has reached 3 μm, their cutoff wavelengths are 1 and 1.5 μm, respectively,³⁷ which indicates that amorphous MoS₂ photodetectors with their much broader photoresponse ranges will have a much wider range of applications. The detectivity (approximately 1×10^7 Jones) may be improved by designing heterostructures based on amorphous MoS₂ and low-dimensional semiconductors such as single-layer MoS₂, graphene, and carbon nanotubes (CNTs).

To have a better understanding of the mechanism underlying the trends exhibited by R_λ and D^* , we measured the absorption spectrum of an amorphous MoS₂ sample with thickness of $T_h = 114.5$ nm with results as shown in Figure 3a. Using Tauc's equation,³⁸ which is expressed as

$$(\alpha h\nu)^n = A(h\nu - E_g) \quad (3)$$

where α is the absorption coefficient, $h\nu$ is the photon energy, A is an energy-independent constant, E_g is the bandgap, and n is equal to 0.5 for the indirect bandgap, a Tauc plot is given in Figure S4 that indicates that the bandgap of amorphous MoS₂ is 0.196 eV, corresponding to a wavelength of 6.34 μm. Unlike many other materials, the absorption line does not show a monotonically downward trend as the wavelength increases but instead exhibits peaks and valleys. When compared with graphene and other narrow bandgap semiconductors, amorphous MoS₂ has fairly high absorbance, which indicates that more incident photons will be converted into electron-hole pairs. In Figure 3a, we selected and marked six points for which the abscissa values are the wavelengths of the light beams used to illuminate the devices, i.e., 473 , 520 , 633 , 973 , 1550 , and 2712 nm, and the red line serves as a guide to the eye. Figure 3b shows a partially enlarged view of the wavelength range from 400 to 1050 nm, in which we can observe the trends more clearly. The sharp drop in the absorption line at a wavelength of 860 nm is due to a change in the optical grating in the UV-visible (UV-vis) spectrometer, but it has no impact on the analysis. By combining the red line in Figure 3a with the lines shown in Figure 2c, we find that they exhibit the same trends as the wavelength increases, which indicates that the high R_λ and D^* result from high absorbance. It is easy to understand that higher light absorbance results in more photons being converted into electron-hole pairs and thus a higher photocurrent, which means larger R_λ and D^* .

values. The absorption line shows an upward trend even at wavelengths over $2.7 \mu\text{m}$, which means that high R_λ and D^* values can be obtained.

Furthermore, amorphous MoS_2 samples with different thicknesses ranging from 13.3 to 114.5 nm were prepared to explore the relationship between photoresponse characterization and sample thickness. Illuminated by light at a wavelength of 1550 nm ($P_{\text{opt}} = 4 \text{ mW}$), we recorded the photocurrents of samples of different thicknesses under bias voltages ranging from -1 to 1 V , as shown in Figure 4a. Using Equations 1, R_λ at $V_{\text{ds}} = 1 \text{ V}$ can be derived from the above results and the calculated values are shown in Figure 4b. We find that as the thickness increases from 13.3 to 114.5 nm, R_λ also increase monotonically. This occurs because when the thickness increases, the incident light will be absorbed more sufficiently and thus more photons will be converted into electron–hole pairs, which results in higher photocurrents and thus larger R_λ values. To demonstrate the spatial uniformity of photodetectors, almost 5600 photodetectors were simultaneously prepared by magnetron sputtering on a $5 \times 5 \text{ cm}$ SiO_2/Si wafer and we measured the thicknesses of channels and photocurrents of 21 photodetectors in two perpendicular areas, with results as shown in Figure S5. The average photocurrent (I_{ph}) and thickness (T_{h}) are $17.10 \mu\text{A}$ and 24.16 nm , while the ranges of photocurrent and thickness are $\Delta I_{\text{ph}} = 0.86 \mu\text{A}$ and $\Delta T_{\text{h}} = 0.90 \text{ nm}$. Thus, $\Delta I_{\text{ph}}/I_{\text{ph}}$ and $\Delta T_{\text{h}}/T_{\text{h}}$ are 5.03% and 3.73% respectively, which demonstrates excellent spatial uniformity of photodetectors. Figure 4c shows the R_λ and D^* values of the amorphous MoS_2 samples when the bias voltage increases to -10 V . R_λ reaches as high as 47.5 mA W^{-1} at $V_{\text{ds}} = -10 \text{ V}$ and $\lambda = 1550 \text{ nm}$, which is higher than the corresponding value of the polycrystalline $\text{MoS}_{1.89}$ photodetectors that were prepared by PLD ($R_\lambda \approx 32 \text{ mA W}^{-1}$ at $V_{\text{ds}} = -10 \text{ V}$, and $\lambda = 1550 \text{ nm}$).³⁴ Higher bias voltages lead to higher carrier drift velocities, reduced carrier transit times and thus higher photocurrent and photoresponsivity values. To explore the relationship between the photocurrent and the incident light power, we used 1550 nm light to illuminate the device and we recorded the photoresponse of a 43 nm-thick amorphous MoS_2 sample under various light powers from 2 to 11 mW, with results as shown in Figure 4d and Figure S6. As shown in Figure 4d, the relationship between the photocurrent and the incident light power is consistent with the power law ($I_{\text{ph}} = AP^\theta$, $\theta = 0.96$) with excellent linearity, thus demonstrating the excellent photocurrent capability of the proposed device. The time dependence of the photocurrent when measured under illumination at a wavelength of 520 nm and a bias voltage of $V_{\text{ds}} = 1 \text{ V}$ is shown in Figure 4e, f and Figure S7. The rise time (τ_{rise}) is defined as the time for photocurrent to rise from 10% to 90% of the pulse peak, while the decay time (τ_{decay}) is defined as the time for photocurrent to decline from 90% to 10% of the pulse peak. Under illumination by an incident light beam with a large spot, the photocurrent increased fastly to the pulse peak. But meanwhile, the device and the substrate were heated all the time, which resulted in a slow and continuous rise in the current within the range to the right of the red dashed line shown in Figure 4e. Similarly, when the light was switched off, the photocurrent declined quickly to the pulse nadir and the temperatures of both device and substrate continued to fall simultaneously, which accounts for the slow but continuous decline in the current in the range to the right of the red dashed line shown in Figure 4f. So when the light was switched

on, the pulse peak is the intersection of the photocurrent curve and the red dashed line in the Figure 4e. The device shows fast response times of $\tau_{\text{rise}} = 10 \text{ ms}$ and $\tau_{\text{decay}} = 16 \text{ ms}$ for the rise and decay times, respectively. The influence of sputtering process parameters on performance of a- MoS_2 photodetectors is shown in Figure S8. We found that the RF power and pressure can significantly affect the material's properties and the underlying mechanism will be discussed in the next section.

The amorphous MoS_2 prepared by magnetron sputtering demonstrates an ultrabroadband response from 473 to 2712 nm and has a narrow bandgap of 0.196 eV, which breaks through the intrinsic bandgap of crystalline MoS_2 . Amorphous MoS_2 is a highly disordered system in which large numbers of dangling bonds exist as defects that can pin the Fermi level (E_{F}), which also indicates that the properties of amorphous MoS_2 are quite different from those of crystalline MoS_2 . To explain the underlying mechanism of the ultrabroadband response of amorphous MoS_2 , we suppose that the neutral dangling bonds, denoted by D^0 , have unpaired electrons and can lose or gain another single electron, denoted by D^+ and D^- , respectively. According to Anderson's theory,³⁹ when the electron occupation of these dangling bonds changes, lattice distortion will occur, and if the energy reduction caused by the lattice distortion is higher than the energy augmentation from Coulomb repulsion, then the correlation energy U can be negative. We assume that the reaction, which can be expressed as



is exothermic and can take place spontaneously. The reaction is depicted in Figure 5a, in which the horizontal axis represents

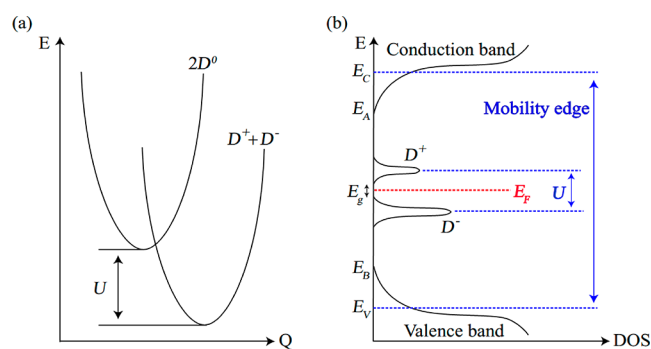


Figure 5. Diagram of ultrabroadband response mechanism of a- MoS_2 photodetectors. (a) Configurational coordinate diagram for $2D^0$ and $D^+ + D^-$ states. (b) Hypothetical energy band diagram of amorphous MoS_2 .

the configuration of the atoms near the defects, whereas the vertical axis represents the gross system energy. The two curves represent the two electronic states of $2D^0$ and $D^+ + D^-$. The minimum energy in the right curve is lower than that in the left curve, which means that the system has lower energy in the $D^+ + D^-$ state and all defects should be either D^+ or D^- . Therefore, the D^0 state only occurs when an electron is excited from D^- to the D^+ band. The density of states (DOS) in the D^+ and D^- band is proportional to the number of defects, N_{D^+} and N_{D^-} . If there are no other donor or acceptor impurities in the amorphous MoS_2 , these quantities are expected to be equal. From the discussion above, the hypothetical energy band of amorphous MoS_2 can be depicted as shown in Figure 5b. E_{C} and E_{V} define the mobility edges and the mobility gap

(i.e., $\Delta E = E_C - E_V$). $\Delta E_1 (= E_C - E_A)$ and $\Delta E_2 (= E_B - E_V)$ are energy ranges in which states are localized because of the absence of long-range order in amorphous MoS₂.⁴⁰ E_g is the bandgap between the D^- and D^+ bands and it can have a fairly small value because of the small correlation energy U . Transitions from the valence band to the D^+ band, from the D^- band to the conduction band and from the D^- to the D^+ band can successfully account for the spectral response when the photon energy is lower than the mobility bandgap or the intrinsic bandgap of crystalline MoS₂. Because the optoelectronic and electronic properties of amorphous MoS₂ are strongly correlated to the defects, the RF power and the pressure can affect the defect density and can thus affect the properties of amorphous MoS₂; this can successfully account for the dependences of the photoresponse characterizations on RF power and pressure.

As shown in Table 1, the amorphous MoS₂ photodetectors exhibit the highest photoresponsivity and a relatively quite

Table 1. Performance Comparison of Our Devices with Some Recently Reported Devices

material	spectral range (nm)	responsivity (mA W ⁻¹)	detectivity (Jones)	ref
a-MoS ₂	473–2712	47.5	1.26×10^7	this work
MoS _{1.89}	445–2717	32	1×10^9	34
MoS _{2.15}	445–9536	21.8		35
WS ₂ /Si	365–1000	4	1.5×10^{10}	41
MoS ₂ /graphene	650	32		42
MoS ₂ /CdTe	200–1700	36.6	6.1×10^{10}	43
α -CsPbI ₃	400–700	35	1.8×10^{12}	44
WS ₂ /MoS ₂	532	4.36	4.4×10^{13}	45

wide spectral range from 473 to 2712 nm. Although the MoS_{2.15} photodetectors exhibit a wider spectral range than our devices, but our devices show a much higher photoresponsivity than the MoS_{2.15} photodetectors.³⁵ The high photoresponsivity and wide spectral range indicate that the amorphous MoS₂ photodetectors has significant potential for electronic and optoelectronic applications. Furthermore, the photoresponsivity and detectivity may be further improved by combining the amorphous MoS₂ with low-dimensional semiconductors such as single-layer MoS₂, graphene, and carbon nanotubes (CNTs).

3. CONCLUSION

In summary, in association with a narrow bandgap of 0.196 eV that originates from defects, amorphous MoS₂ photodetectors are prepared by the magnetron sputtering technique. These photodetectors have realized an ultrabroadband response from 473 to 2712 nm at room temperature, with photoresponsivity reaching as high as 47.5 mA W⁻¹. With its advantage of fairly high absorbance over a broad spectral range when compared with graphene and other narrow bandgap semiconductors, amorphous MoS₂ has the ability to convert light into electronic signals more satisfactorily. Because of the superiority of the magnetron sputtering technique, it can readily achieve large-scale device fabrication with high yield at ultralow cost, which indicates the wide applicability of amorphous MoS₂ in the electronic and optoelectronic fields, including imaging, communications, and broadband detection applications. The use of energy gap engineering combined with the amorphous

structure and defects represents a quite promising way to search for high-performance photoelectric materials and forms an attractive research area for next-generation electronic and optoelectronic devices.

4. METHODS

Sample Preparation and Characterization. Amorphous MoS₂ was fabricated by the magnetron sputtering system (Anelva L-332S-FHL Sputtering system). The X-ray photoelectron spectroscopy (XPS) spectra were measured with a ULVAC-PHI Quantera SXM. The Raman spectra were measured with a Horiba LabRAM HR Raman spectrometer. The Transmission electron microscopy (TEM) and X-ray diffraction (XRD) characterization were performed with a FEI Tecnai F20 TEM and a Rigaku D/max 2500PC X-ray system.

Light Absorption Measurements. The absorption spectra were measured with a PerkinElmer Lambda 950 UV/vis Spectrometer and a Bruker VERTEX 70v Fourier Transform Infrared Spectrometer.

Electrical and Optoelectronic Measurements. Electrical measurements were performed with a semiconductor analyzer (4156C, Agilent, USA) in ambient atmosphere at room temperature. Photoresponse measurements were performed using five semiconductor lasers with wavelength at 473, 520, 633, 973, and 1550 nm and a Fabry–Perot Mid-IR Laser Source with an emission wavelength centered at 2712 nm.

■ ASSOCIATED CONTENT

📄 Supporting Information

The Supporting Information is available free of charge on the ACS Publications website at DOI: 10.1021/acsaem.9b00247.

Fabrication and XPS characterization of amorphous MoS₂ (S1), photoresponse characterization of amorphous MoS₂ using different electrodes (S2), noise spectral density (S3), Tauc plot (S4), spatial uniformity of devices (S5), photoresponse of a 43 nm-thick amorphous MoS₂ sample under varying light power (S6), time-dependent photocurrent measurements under illumination at a wavelength of 520 nm (S7), RF power and pressure dependence of the a-MoS₂ photodetectors (S8), time stability of amorphous MoS₂ photodetectors (S9) (PDF)

■ AUTHOR INFORMATION

Corresponding Author

*E-mail: qunqli@mail.tsinghua.edu.cn.

ORCID

Jiaping Wang: 0000-0002-8300-4992

Qunqing Li: 0000-0001-9565-0855

Notes

The authors declare no competing financial interest.

■ ACKNOWLEDGMENTS

This work was financially supported by the National Key Research and Development Program of China (2017YFA0205800) and the National Natural Science Foundation of China (51532008, 11574171, 51472141).

■ REFERENCES

- (1) Choe, J.-W.; O, B.; Bandara, K. M. S. V.; Coon, D. D. Exchange Interaction Effects in Quantum Well Infrared Detectors and Absorbers. *Appl. Phys. Lett.* **1990**, *56*, 1679–1681.
- (2) Palaferri, D.; Todorov, Y.; Bigioli, A.; Mottaghizadeh, A.; Gacemi, D.; Calabrese, A.; Vasaneli, A.; Li, L.; Davies, A. G.; Linfield, E. H.; et al. Room-Temperature Nine- μ m-Wavelength Photodetectors

- and GHz-Frequency Heterodyne Receivers. *Nature* **2018**, *556*, 85–88.
- (3) Konstantatos, G.; Howard, I.; Fischer, A.; Hoogland, S.; Clifford, J.; Klem, E.; Levina, L.; Sargent, E. H. Ultrasensitive Solution-Cast Quantum Dot Photodetectors. *Nature* **2006**, *442*, 180–183.
- (4) Meredith, P.; Bettinger, C. J.; Irimia-Vladu, M.; Mostert, A. B.; Schwenn, P. E. Electronic and Optoelectronic Materials and Devices Inspired by Nature. *Rep. Prog. Phys.* **2013**, *76*, 034501.
- (5) Yang, G.; Gu, Y.; Yan, P.; Wang, J.; Xue, J.; Zhang, X.; Lu, N.; Chen, G. Chemical Vapor Deposition Growth of Vertical MoS₂ Nanosheets on P-GaN Nanorods for Photodetector Application. *ACS Appl. Mater. Interfaces* **2019**, *11*, 8453–8460.
- (6) Yang, W.; Hu, K.; Teng, F.; Weng, J.; Zhang, Y.; Fang, X. High-Performance Silicon-Compatible Large-Area UV-to-Visible Broadband Photodetector Based on Integrated Lattice-Matched Type II Se/n-Si Heterojunctions. *Nano Lett.* **2018**, *18*, 4697–4703.
- (7) Fang, X.; Hu, L.; Huo, K.; Gao, B.; Zhao, L.; Liao, M.; Chu, P. K.; Bando, Y.; Golberg, D. New Ultraviolet Photodetector Based on Individual Nb₂O₅ Nanobelts. *Adv. Funct. Mater.* **2011**, *21*, 3907–3915.
- (8) Yang, W.; Chen, J.; Zhang, Y.; Zhang, Y.; He, J. H.; Fang, X. Silicon-Compatible Photodetectors: Trends to Monolithically Integrate Photosensors with Chip Technology. *Adv. Funct. Mater.* **2019**, *29*, 1808182.
- (9) Bannur, B.; K. N., H.; Rao, K. D. M.; Kulkarni, G. U. Solution-Based Fast Fabrication of a High-Performance Unlimited Area Au Nanostructure/Si Heterojunction Photodetector. *ACS Appl. Electron. Mater.* **2019**, *1*, 577–584.
- (10) Hu, L.; Yan, J.; Liao, M.; Xiang, H.; Gong, X.; Zhang, L.; Fang, X. An Optimized Ultraviolet-a Light Photodetector with Wide-Range Photoresponse Based on ZnS/ZnO Biaxial Nanobelt. *Adv. Mater.* **2012**, *24*, 2305–2309.
- (11) O'Brien, G. A.; Quinn, A. J.; Tanner, D. A.; Redmond, G. A. Single Polymer Nanowire Photodetector. *Adv. Mater.* **2006**, *18*, 2379–2383.
- (12) Pospischil, A.; Humer, M.; Furchi, M. M.; Bachmann, D.; Guider, R.; Fromherz, T.; Mueller, T. CMOS-Compatible Graphene Photodetector Covering All Optical Communication Bands. *Nat. Photonics* **2013**, *7*, 892–896.
- (13) Jeong, I. S.; Kim, J. H.; Im, S. Ultraviolet-Enhanced Photodiode Employing n-ZnO/p-Si Structure. *Appl. Phys. Lett.* **2003**, *83*, 2946–2948.
- (14) Tang, L.; Kocabas, S. E.; Latif, S.; Okyay, A. K.; Ly-Gagnon, D. S.; Saraswat, K. C.; Miller, D. A. B. Nanometre-Scale Germanium Photodetector Enhanced by a near-Infrared Dipole Antenna. *Nat. Photonics* **2008**, *2*, 226–229.
- (15) Lou, Z.; Zeng, L.; Wang, Y.; Wu, D.; Xu, T.; Shi, Z.; Tian, Y.; Li, X.; Tsang, Y. H. High-Performance MoS₂/Si Heterojunction Broadband Photodetectors from Deep Ultraviolet to near Infrared. *Opt. Lett.* **2017**, *42*, 3335–3338.
- (16) Zhuo, R.; Wang, Y.; Wu, D.; Lou, Z.; Shi, Z.; Xu, T.; Xu, J.; Tian, Y.; Li, X. High-Performance Self-Powered Deep Ultraviolet Photodetector Based on MoS₂/GaIn p-n Heterojunction. *J. Mater. Chem. C* **2018**, *6*, 299–303.
- (17) Wu, E.; Wu, D.; Jia, C.; Wang, Y.; Yuan, H.; Zeng, L.; Xu, T.; Shi, Z.; Tian, Y.; Li, X. In Situ Fabrication of 2D WS₂/Si Type-II Heterojunction for Self-Powered Broadband Photodetector with Response up to Mid-Infrared. *ACS Photonics* **2019**, *6*, 565–572.
- (18) Xiao, P.; Mao, J.; Ding, K.; Luo, W.; Hu, W.; Zhang, X.; Zhang, X.; Jie, J. Solution-Processed 3D RGO–MoS₂/Pyramid Si Heterojunction for Ultrahigh Detectivity and Ultra-Broadband Photodetection. *Adv. Mater.* **2018**, *30*, 1801729.
- (19) Zhao, Z. M.; Jiang, R. L.; Chen, P.; xi, D. J.; Luo, Z. Y.; Zhang, R.; Shen, B.; Chen, Z. Z.; Zheng, Y. D. Metal–semiconductor–metal GaN Ultraviolet Photodetectors on Si(111). *Appl. Phys. Lett.* **2000**, *77*, 444–446.
- (20) Kim, H. Y.; Kim, J. H.; Kim, Y. J.; Chae, K. H.; Whang, C. N.; Song, J. H.; Im, S. Photoresponse of Si Detector Based on N-ZnO/p-Si and n-ZnO/n-Si Structures. *Opt. Mater. (Amsterdam, Neth.)* **2001**, *17*, 141–144.
- (21) Lao, Y. F.; Perera, A. G. U.; Li, L. H.; Khanna, S. P.; Linfield, E. H.; Liu, H. C. Tunable Hot-Carrier Photodetection beyond the Bandgap Spectral Limit. *Nat. Photonics* **2014**, *8*, 412–418.
- (22) Norton, P. HgCdTe Infrared Detectors. *Opto-Electronics Rev.* **2002**, *10*, 159–174.
- (23) Ke, Y.; Wang, S.; Liu, G.; Li, M.; White, T. J.; Long, Y. Vanadium Dioxide: The Multistimuli Responsive Material and Its Applications. *Small* **2018**, *14*, 1802025.
- (24) Rogalski, A. Infrared Detectors Status and Trends. *Prog. Quantum Electron.* **2003**, *27*, 59–210.
- (25) Clark, J.; Lanzani, G. Organic Photonics for Communications. *Nat. Photonics* **2010**, *4*, 438–446.
- (26) Wu, D.; Wang, Y.; Zeng, L.; Jia, C.; Wu, E.; Xu, T.; Shi, Z.; Tian, Y.; Li, X.; Tsang, Y. H. Design of 2D Layered PtSe₂ Heterojunction for the High-Performance, Room-Temperature, Broadband, Infrared Photodetector. *ACS Photonics* **2018**, *5*, 3820–3827.
- (27) Chen, H.; Liu, H.; Zhang, Z.; Hu, K.; Fang, X. Nanostructured Photodetectors: From Ultraviolet to Terahertz. *Adv. Mater.* **2016**, *28*, 403–433.
- (28) Tsai, D. S.; Liu, K. K.; Lien, D. H.; Tsai, M. L.; Kang, C. F.; Lin, C. A.; Li, L. J.; He, J. H. Few-Layer MoS₂ with High Broadband Photogain and Fast Optical Switching for Use in Harsh Environments. *ACS Nano* **2013**, *7*, 3905–3911.
- (29) Konstantatos, G.; Badioli, M.; Gaudreau, L.; Osmond, J.; Bernechea, M.; De Arquer, F. P. G.; Gatti, F.; Koppens, F. H. L. Hybrid Graphene-Quantum Dot Phototransistors with Ultrahigh Gain. *Nat. Nanotechnol.* **2012**, *7*, 363–368.
- (30) Deng, W.; Chen, Y.; You, C.; Liu, B.; Yang, Y.; Shen, G.; Li, S.; Sun, L.; Zhang, Y.; Yan, H. High Detectivity from a Lateral Graphene–MoS₂ Schottky Photodetector Grown by Chemical Vapor Deposition. *Adv. Electron. Mater.* **2018**, *4*, 1800069.
- (31) Mak, K. F.; Lee, C.; Hone, J.; Shan, J.; Heinz, T. F. Atomically Thin MoS₂: A New Direct-Gap Semiconductor. *Phys. Rev. Lett.* **2010**, *105*, 136805.
- (32) Yin, Z.; Li, H.; Li, H.; Jiang, L.; Shi, Y.; Sun, Y.; Lu, G.; Zhang, Q.; Chen, X.; Zhang, H. Single-Layer MoS₂ phototransistors. *ACS Nano* **2012**, *6*, 74–80.
- (33) Lopez-Sanchez, O.; Lembke, D.; Kayci, M.; Radenovic, A.; Kis, A. Ultrasensitive Photodetectors Based on Monolayer MoS₂. *Nat. Nanotechnol.* **2013**, *8*, 497–501.
- (34) Xie, Y.; Zhang, B.; Wang, S.; Wang, D.; Wang, A.; Wang, Z.; Yu, H.; Zhang, H.; Chen, Y.; Zhao, M.; et al. Ultrabroadband MoS₂ Photodetector with Spectral Response from 445 to 2717 nm. *Adv. Mater.* **2017**, *29*, 1605972.
- (35) Xie, Y.; Liang, F.; Wang, D.; Chi, S.; Yu, H.; Lin, Z.; Zhang, H.; Chen, Y.; Wang, J.; Wu, Y. Room-Temperature Ultrabroadband Photodetection with MoS₂ by Electronic-Structure Engineering Strategy. *Adv. Mater.* **2018**, *30*, 1804858.
- (36) Wang, X.; Wang, P.; Wang, J.; Hu, W.; Zhou, X.; Guo, N.; Huang, H.; Sun, S.; Shen, H.; Lin, T.; et al. Ultrasensitive and Broadband MoS₂ Photodetector Driven by Ferroelectrics. *Adv. Mater.* **2015**, *27*, 6575–6581.
- (37) Saran, R.; Curry, R. J. Lead Sulphide Nanocrystal Photodetector Technologies. *Nat. Photonics* **2016**, *10*, 81–92.
- (38) Barber, D. B.; Pollock, C. R.; Beecroft, L. L.; Ober, C. K. Amplification by Optical Composites. *Opt. Lett.* **1997**, *22*, 1247–1249.
- (39) Anderson, P. W. Model for the Electronic Structure of Amorphous Semiconductors. *Phys. Rev. Lett.* **1975**, *34*, 953–955.
- (40) Davis, E. A.; Mott, N. F. Conduction in Non-Crystalline Systems V. Conductivity, Optical Absorption and Photoconductivity in Amorphous Semiconductors. *Philos. Mag.* **1970**, *22*, 0903–0922.
- (41) Kim, H. S.; Patel, M.; Kim, J.; Jeong, M. S. Growth of Wafer-Scale Standing Layers of WS₂ for Self-Biased High-Speed UV-Visible-NIR Optoelectronic Devices. *ACS Appl. Mater. Interfaces* **2018**, *10*, 3964–3974.

(42) Chen, C.; Feng, Z.; Feng, Y.; Yue, Y.; Qin, C.; Zhang, D.; Feng, W. Large-Scale Synthesis of a Uniform Film of Bilayer MoS₂ on Graphene for 2D Heterostructure Phototransistors. *ACS Appl. Mater. Interfaces* **2016**, *8*, 19004–19011.

(43) Wang, Y.; Huang, X.; Wu, D.; Zhuo, R.; Wu, E.; Jia, C.; Shi, Z.; Xu, T.; Tian, Y.; Li, X. A Room-Temperature Near-Infrared Photodetector Based on a MoS₂/CdTe p-n Heterojunction with a Broadband Response up to 1700 nm. *J. Mater. Chem. C* **2018**, *6*, 4861–4865.

(44) Sim, K. M.; Swarnkar, A.; Nag, A.; Chung, D. S. Phase Stabilized α -CsPbI₃ Perovskite Nanocrystals for Photodiode Applications. *Laser Photonics Rev.* **2018**, *12*, 1700209.

(45) Wu, W.; Zhang, Q.; Zhou, X.; Li, L.; Su, J.; Wang, F.; Zhai, T. Self-Powered Photovoltaic Photodetector Established on Lateral Monolayer MoS₂-WS₂ Heterostructures. *Nano Energy* **2018**, *51*, 45–53.